

# Ring defects in n-type Czochralski-grown silicon: A high spatial resolution study using Fourier-transform infrared spectroscopy, micro-photoluminescence, and micro-Raman

Rabin Basnet,<sup>1,a)</sup> Chang Sun,<sup>1</sup> Huiting Wu,<sup>1</sup> Hieu T. Nguyen,<sup>1</sup> Fiacre Emile Rougieux,<sup>2</sup> and Daniel Macdonald<sup>1</sup>

<sup>1</sup>Research School of Engineering, The Australian National University, Canberra, Australian Capital Territory 2601, Australia

<sup>2</sup>School of Photovoltaic and Renewable Energy Engineering, The University of New South Wales, Sydney, New South Wales, Australia

(Received 15 September 2018; accepted 6 December 2018; published online 26 December 2018)

We investigated ring defects induced by a two-step anneal in n-type Czochralski-grown silicon wafers using a combination of high spatial resolution Fourier Transform Infrared Spectroscopy (FTIR), micro-photoluminescence (PL) mapping, and micro-Raman mapping. Through FTIR measurements, we show the inhomogeneous loss in interstitial oxygen with a positive correlation with the inverse lifetime. Using high-resolution micro-PL mapping, we are able to distinguish individual recombination-active oxygen precipitates within the rings with a decreasing density from the center to the edge of the sample. The radial inhomogeneity of the oxygen precipitates is likely to be related to variations in the distribution of grown-in defects. We also demonstrate that micro-Raman mapping reveals the oxygen precipitates without the smearing effects of carrier diffusion that are present in micro-PL mapping. *Published by AIP Publishing.* <https://doi.org/10.1063/1.5057724>

## I. INTRODUCTION

N-type Czochralski-grown silicon (Cz-Si) is the most common material used for high-efficiency crystalline silicon solar cells. During certain high-temperature treatments, Cz-Si wafers sometimes develop ring defects which influence the uniformity of the electrical properties of the wafer.<sup>1,2</sup> Ring defects are usually associated with the inhomogeneous distribution of oxygen precipitates and their associated extended defects.<sup>1–3</sup> Ring defects can contribute up to 4% (absolute) loss in solar cell efficiency<sup>4</sup> owing to the strong recombination activity of these oxygen precipitates.<sup>5–7</sup> However, a detailed understanding of the origin and properties of ring defects remains incomplete. Improved techniques to observe and quantify the recombination active precipitates within the ring defects will help to further improve this understanding.

It is known that the interstitial oxygen concentration  $[O_i]$  distribution during ingot growth affects the formation of micro-defects.<sup>8,9</sup> Nauka *et al.*<sup>10</sup> observed a quantitative relationship between the  $[O_i]$  distribution and the excess carrier lifetime, in as-grown Cz-Si along the crystal growth direction. Similarly, Varker *et al.*<sup>11</sup> observed the inhomogeneous distribution of minority carrier lifetime along the radial direction after two-step annealing, in Cz-Si wafers. More recently, Gaspar *et al.*<sup>12</sup> demonstrated that the initial radial distribution of  $[O_i]$  has an influence on the radial distribution of the minority carrier lifetime at the millimeter (mm) scale. Previous work has used Fourier Transform Infrared Spectroscopy (FTIR) to measure the  $[O_i]$  concentration with mm scale spatial resolution.<sup>12</sup> In this work, we investigate the distribution of the  $[O_i]$  concentration at the sub-mm scale using an FTIR scanning microscope. We show

that the high resolution  $[O_i]$  scans are well correlated with photoluminescence (PL) based images of the carrier lifetime on n-type Cz wafers subjected to a two-step anneal.

PL imaging yields lifetime images with a spatial resolution in the 10–100  $\mu\text{m}$  range, and the relatively low injection level achieved during PL imaging results in significant image smearing due to the lateral diffusion of carriers, which typically extends many tens of micrometers.<sup>13</sup> As a result, ring defects appear as continuous bands of a reduced lifetime in PL images under constant and homogenous laser excitation, as has been reported by numerous authors.<sup>4,14</sup> To address these problems, we have utilized a micro-PL system with confocal optics with a higher spatial resolution, in principle down to 1  $\mu\text{m}$  based on the optical configuration. In addition, a much higher injection level can be achieved, which makes the carrier lifetime largely Auger limited<sup>15–17</sup> and reduces carrier smearing effects during measurements. However, in practice, carrier smearing effects are still present and limit the achievable spatial resolution to several micrometers. Furthermore, micro-PL only detects those particles that are strongly recombination active. To further improve the spatial resolution, we also applied micro-Raman mapping. The Raman signal from crystalline silicon is very sensitive to defects and impurities in the material such as dislocations, metal precipitates, and doping densities.<sup>18,19</sup> We will utilize the spatial resolution below 1  $\mu\text{m}$  to observe the oxygen precipitates and demonstrate that the two mapping techniques are complementary to each other.

## II. EXPERIMENTAL DETAILS

### A. Sample preparation

The samples used in this work were quartered sections of 4-in. diameter, 275  $\mu\text{m}$  thick, phosphorus doped,

<sup>a)</sup>E-mail: rabin.basnet@anu.edu.au

electronic-grade Cz-Si wafers with a resistivity of  $1\ \Omega\text{ cm}$ . Samples were divided into two different groups; Group I—for the FTIR measurements and Group II—for the micro-PL and micro-Raman mappings. The samples from Group I were saw-damage etched with tetramethylammonium hydroxide (TMAH) solution and samples from Group II were chemically ( $\text{HNO}_3\text{:HF } 10\text{:}1$ ) etched to remove  $10\text{--}12\ \mu\text{m}$  from each side, before standard chemical cleaning steps prior to further processing. Oxygen precipitates were grown intentionally by subjecting the samples from both groups to a low-high, two-step anneal process. First, the samples were annealed at  $650\ ^\circ\text{C}$  for 5 h in nitrogen for the nucleation of the oxygen precipitates.<sup>20</sup> Subsequently, in the second step, the samples were annealed at  $1000\ ^\circ\text{C}$  for 11 h in oxygen for the growth of the oxygen precipitates.<sup>20</sup> Further, some samples from Group II were annealed at  $1000\ ^\circ\text{C}$  for an additional 4 h (total 15 h). After annealing, the Group II samples were chemically ( $\text{HNO}_3\text{:HF } 10\text{:}1$ ) etched to remove several micrometers of silicon and any denuded zone,<sup>21</sup> before characterization. We note that these annealing conditions are indeed not typical for solar cell processing, but they were chosen in this work to ensure a high precipitate density to enable a clear demonstration of the methods.

To allow the measurement of PL images and micro-PL maps, all samples were passivated with thermal aluminum oxygen ( $\text{Al}_2\text{O}_3$ ) layers deposited on both sides using a Beneq TFS-200 atomic layer deposition (ALD) system.

### B. FTIR scanning

In this study, radial distributions of  $[\text{O}_i]$  were measured by line scans before and after annealing, with a step size of  $160\ \mu\text{m}$  using a Bruker Vertex 80 FTIR microscope equipped with the liquid-nitrogen-cooled InGaAs detector. The FTIR line scans were conducted after removing oxide layers of annealed samples using a laser spot size of  $10\ \mu\text{m}$  and a spectral resolution of  $4\ \text{cm}^{-1}$ . In general, the broad infrared absorption band near  $1107\ \text{cm}^{-1}$  at room temperature has been ascribed to  $[\text{O}_i]$ .<sup>22</sup> During scanning, room temperature transmission measurements were performed in the range from  $500$  to  $2500\ \text{cm}^{-1}$ . The transmission spectra obtained from the FTIR measurements were corrected by filtering out high-frequency oscillations via wavelet transformation. In order to extract the relative  $[\text{O}_i]$  from the corrected transmission spectra, a baseline value was constructed, being an expected transmission spectrum in the absence of interstitial oxygen. The uncertainties in the  $[\text{O}_i]$  measurements arise mainly from variations in the wafer thickness and overlapping of the interstitial oxygen peak and the oxygen precipitate band and are estimated to be approximately 10%. The relative  $[\text{O}_i]$  values extracted from the FTIR measurements were converted to absolute  $[\text{O}_i]$  concentrations by using SEMI MF standard 1188-1107.

### C. PL imaging

PL images were obtained using an LIS-R1 PL imaging tool from BT imaging.<sup>23</sup> The pixel sizes of the PL images were approximately  $162\ \mu\text{m}$  and  $23\ \mu\text{m}$  for the standard and

the magnifying lenses, respectively. The injection level was estimated to be in the range of  $10^{15}\text{--}10^{16}\ \text{cm}^{-3}$ .

### D. Micro-PL and micro-Raman mapping

In this work, both the micro-PL and the micro-Raman maps were obtained at room temperature using a Horiba LabRam HR Evolution system equipped with a confocal microscope. The samples were excited with a  $532\ \text{nm}$  continuous-wave laser focused onto a spot size of  $1.2\ \mu\text{m}$  in diameter with a  $50\times$  objective lens. The laser power on the sample surface was  $19\ \text{mW}$ .

Micro-PL maps were obtained using a liquid-nitrogen-cooled InGaAs array detector and a step size (pixel size) of  $2\ \mu\text{m}$  in both  $x$  and  $y$  directions. The band-to-band transition of free carriers in silicon is represented as a peak at around  $1130\ \text{nm}$ . The intensity maps of the samples were obtained by integrating the luminescence intensity across the wavelength range from  $1050$  to  $1200\ \text{nm}$ . At room temperature, the absorption depth of the  $532\ \text{nm}$  laser light is around  $1.2\ \mu\text{m}$ .<sup>24</sup> The apparent precipitate density calculated from the micro-PL maps was expressed as an average areal density, to avoid the uncertainty of estimating the detection depth that would be required to estimate a volume density. The detection depth will be somewhat deeper than the absorption depth due to the diffusion of excess carriers, which is estimated to be several micrometers in magnitude. The injection level during micro-PL mapping was estimated to be around  $10^{18}\ \text{cm}^{-3}$ .

Micro-Raman maps were obtained using a silicon charge coupled device (CCD) detector to detect the backscattered Raman light. In the absence of either internal or external stress, crystalline silicon has a Raman peak at  $520\ \text{cm}^{-1}$ . We mapped the intensity of this peak with a step-size of  $0.5\ \mu\text{m}$  in both  $x$  and  $y$  directions.

## III. RESULTS AND DISCUSSION

### A. The loss in $[\text{O}_i]$

Figure 1 presents the radial distributions of  $[\text{O}_i]$  in both the as-grown and the Group I ( $11\ \text{h}$  annealed) samples,

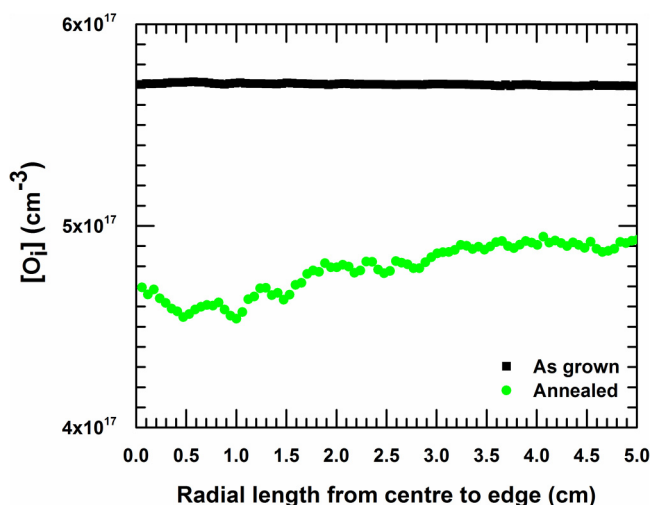


FIG. 1. FTIR measured radial distribution of  $[\text{O}_i]$  for the as-grown sample and the Group I sample ( $650\ ^\circ\text{C}$ -5 h;  $1000\ ^\circ\text{C}$ -11 h).

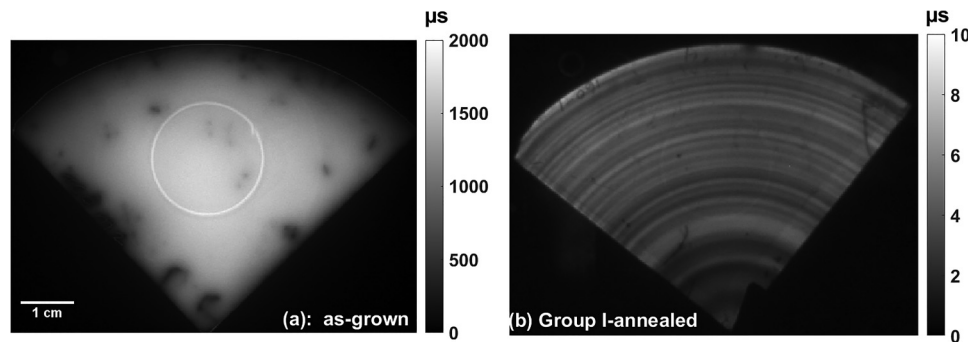


FIG. 2. PL based carrier lifetime images of the (a) as-grown sample and the Group I sample (650 °C-5 h; 1000 °C-11 h). The PL images were captured at an average injection level of  $\Delta p = 5 \times 10^{13} \text{ cm}^{-3}$ . The bright circle in the images is an artifact due to the conductance coil in the PL imaging tool.

measured from the center to the edge of the samples. It shows that in the as-grown sample, the  $[O_i]$  distribution is very uniform along the radial direction. However, in the annealed sample, we observed a strongly non-uniform distribution of  $[O_i]$ —lower toward the center in comparison to the edge of the sample, and with mm-scale local variations. The loss in  $[O_i]$  can be determined by  $\Delta[O_i] = [O_i]_{\text{as-grown}} - [O_i]_{\text{annealed}}$ , and indicates the magnitude of oxygen precipitation in the samples. Note that the solubility limit of interstitial oxygen in silicon at 1000 °C in an oxygen ambient is around  $9 \times 10^{16} \text{ cm}^{-3}$ ,<sup>11</sup> significantly lower than the concentrations measured here, creating a strong driving force for precipitation. In general, the loss in  $[O_i]$  is expected to depend on both the initial  $[O_i]$  content and the thermal treatment.<sup>25</sup> Further, oxygen precipitation is enhanced by the presence of vacancies in the crystal.<sup>26</sup> Based on Voronkov's theory,<sup>27</sup> the type of intrinsic point defect (vacancies and silicon interstitial) in a crystal depends on the so-called V/G criterion (where V is the crystal growth rate and G is the radial temperature gradient). In principle, the relatively fast growth rates used for commercial silicon ingots result in a relatively vacancy-rich crystal.<sup>26</sup> This usually results in a radial vacancy gradient which decreases toward the edge,<sup>28</sup> leading to less oxygen precipitation and a lower loss of  $[O_i]$  toward the edge, as we observed in the annealed sample shown in Fig. 1.

Further, we observed mm-scale local fluctuations in the loss in  $[O_i]$  in the annealed sample. This is also likely to be related to the crystal growth conditions, where small temperature deviations can occur in the melt and at the crystal growth interface due to variations in thermal convection, crystal rotation, and crystal pull rate.<sup>29,30</sup> These temperature variations cause microscopic growth rate fluctuations, as a result of which impurities such as dopants, oxygen, and carbon are inhomogeneously incorporated into the growing crystal.<sup>31–34</sup> The inhomogeneously distributed impurities in the crystal can trigger clustering of intrinsic point defects (vacancies and silicon interstitials) and induced agglomeration of supersaturated oxygen during cooling down.<sup>35</sup> This leads to an inhomogeneous incorporation of grown-in oxygen precipitate nuclei and subsequently induces local fluctuations in the loss of  $[O_i]$  during annealing.

## B. The loss in $[O_i]$ and carrier lifetime

Figure 2 shows PL-based lifetime images of both the as-grown and the Group I samples, expressed as effective carrier lifetimes via calibration with a photoconductance

coil.<sup>23</sup> The as-grown sample shows a uniform and high average lifetime ( $\tau_{\text{as-grown}}$ ) of 1880  $\mu\text{s}$ , as shown in Fig. 2(a). Note that the dark spots in this image are surface artifacts. However, after the two-step anneal, ring defects were formed which caused lifetime striations, and the average minority carrier lifetime ( $\tau_{\text{annealed}}$ ) had degraded to approximately 5  $\mu\text{s}$ , as shown in Fig. 2(b). All PL images are shown at an average injection level of around  $\Delta p = 5 \times 10^{13} \text{ cm}^{-3}$  by varying the illumination intensity.

Figure 3 shows the radial profiles of the loss in  $[O_i]$  and the inverse carrier lifetime for the Group I (11 h annealed) sample. Note that for an approximately equal excess carrier density, the inverse lifetime is approximately proportional to the effective defect concentration, and represents the recombination strength of the defects at a given location. Both the loss in  $[O_i]$  and the inverse lifetime profiles were measured with the same spatial resolution of 160  $\mu\text{m}$ . We observed clear correlations, both globally across the sample and at the local scale, between the amount of interstitial oxygen loss and the inverse lifetime, as shown in Fig. 3. This result further supports the conclusion that the lifetime striations are due to the local fluctuations of oxygen precipitates originating from grown-in precipitate nuclei as explained in Sec. III A. Thus, dissolving the grown-in oxygen precipitate nuclei by a high-temperature pre-annealing step known as a *tabula rasa* can be expected to mitigate the formation of the

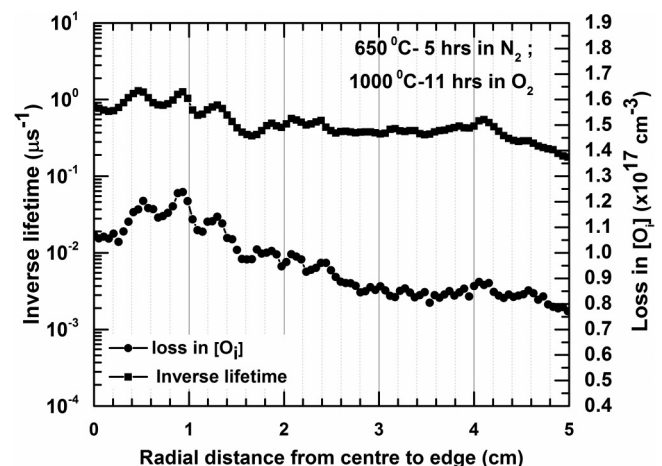


FIG. 3. Microscale radial distribution of the inverse lifetime extracted from PL image and loss in  $[O_i]$  obtained from FTIR measurements in a Group I sample (650 °C-5 h; 1000 °C-11 h).



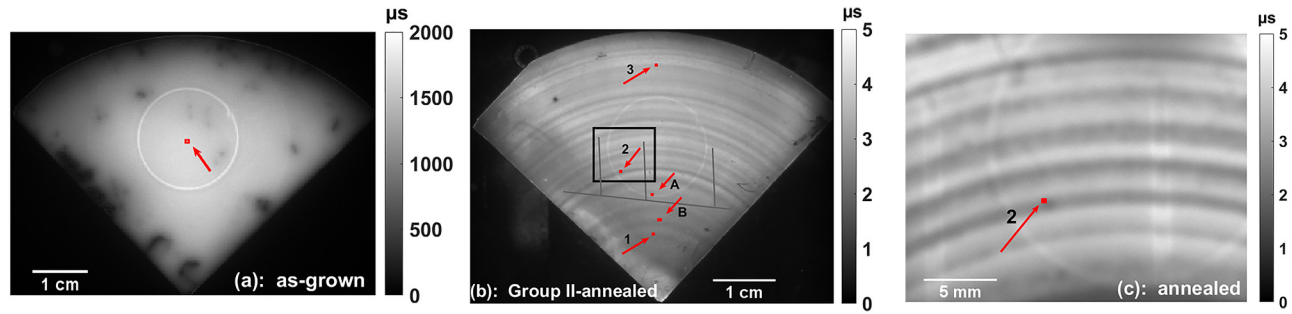


FIG. 4. PL based carrier lifetime images of the (a) as-grown sample and the Group II sample ( $650\text{ }^{\circ}\text{C}$ -5 h;  $1000\text{ }^{\circ}\text{C}$ -15 h) captured with (b) standard lens (pixel size of  $162\text{ }\mu\text{m}$ ) and (c) magnifying lens (pixel size of  $23\text{ }\mu\text{m}$ ). The PL images were captured at an average injection level of  $\Delta p = 5 \times 10^{13}\text{ cm}^{-3}$ . The red points indicate the locations (not the size) of the micro-PL maps in this work. The black box in (b) indicates the area of the PL image captured with the magnifying lens shown in (c). The bright circle in the images is an artifact due to the conductance coil in the PL imaging tool. The straight lines in (b) and (c) are laser marks for locating specific regions.

ring defects in subsequent thermal treatments, as has been demonstrated by previous research work.<sup>36</sup>

### C. PL images, micro-PL maps, and apparent oxygen precipitate density

Figure 4 shows the PL-based lifetime images of the as-grown sample with a standard lens and the Group II sample with both standard and magnifying lenses expressed as effective carrier lifetimes via calibration with a photoconductance coil.<sup>23</sup>

Figure 5 shows the micro-PL maps of the as-grown and the Group II ( $650\text{ }^{\circ}\text{C}$ -5 h;  $1000\text{ }^{\circ}\text{C}$ -15 h) samples. The mapped areas in the samples are indicated by red points in Fig. 4, although they are not to scale. In the as-grown sample, no

individual recombination sites were observed, whereas, in the annealed sample, heterogeneously distributed individual recombination sites were detected, as shown in Fig. 5. The recombination sites appear to be sub-micrometer sized and are closely spaced as a result; the conventional PL images were not able to resolve them. However, the micro-PL maps successfully resolved the individual recombination sites due to the use of a pixel size of  $2\text{ }\mu\text{m}$  and a much higher injection level. Therefore, we were able to demonstrate that ring defects are in fact a cumulative effect of the individual recombination sites rather than continuous bands, as observed in the PL images in Figs. 4(b) and 4(c). In this work, we found randomly distributed oxygen precipitates with a higher apparent areal density of  $9 \times 10^9\text{ cm}^{-2}$  at position 1, as shown in the map in Fig. 5(b). Similarly, at position 2, we found more

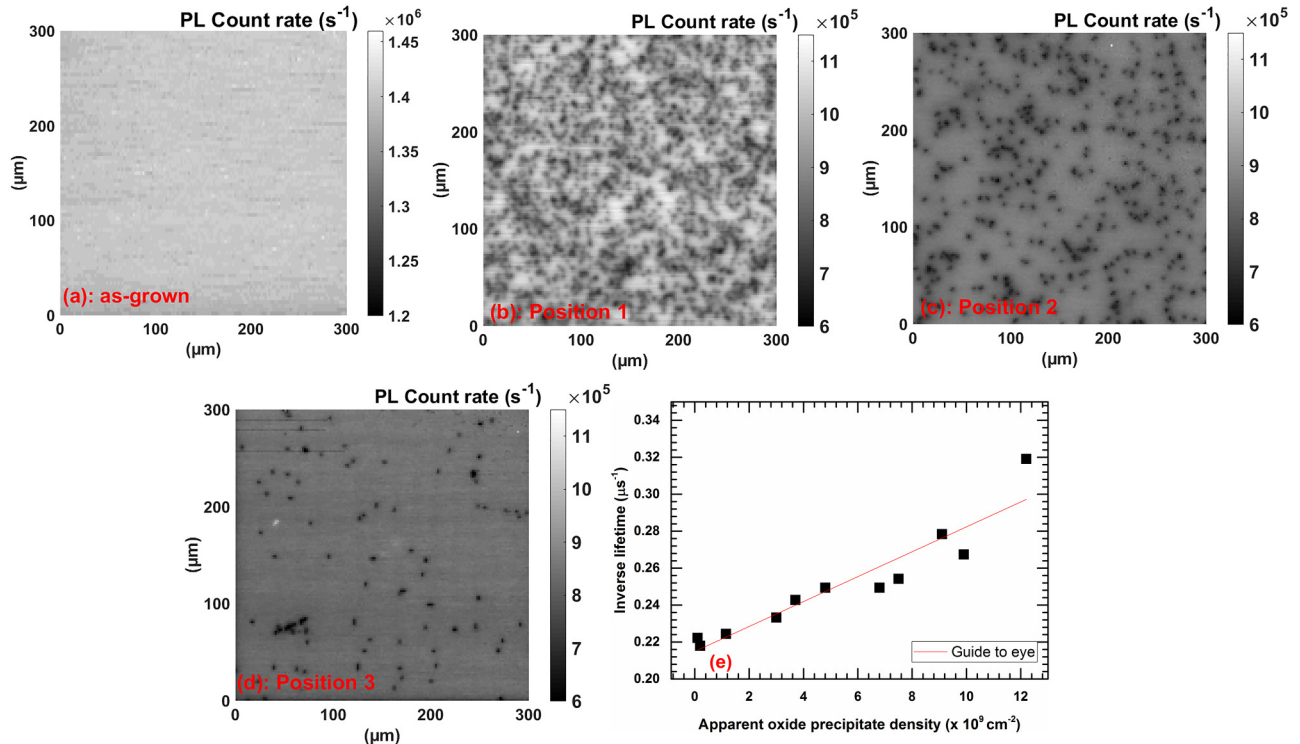


FIG. 5. Micro-PL maps of  $300\text{ }\mu\text{m} \times 300\text{ }\mu\text{m}$  areas on (a) the as-grown sample and [(b)–(d)] on the Group II sample ( $650\text{ }^{\circ}\text{C}$ -5 h;  $1000\text{ }^{\circ}\text{C}$ -15 h). The locations of the micro-PL maps are indicated in the PL images in Fig. 4. (e) Inverse lifetime extracted from the PL image as a function of apparent oxygen precipitate areal density obtained from micro-PL maps on the Group II sample.

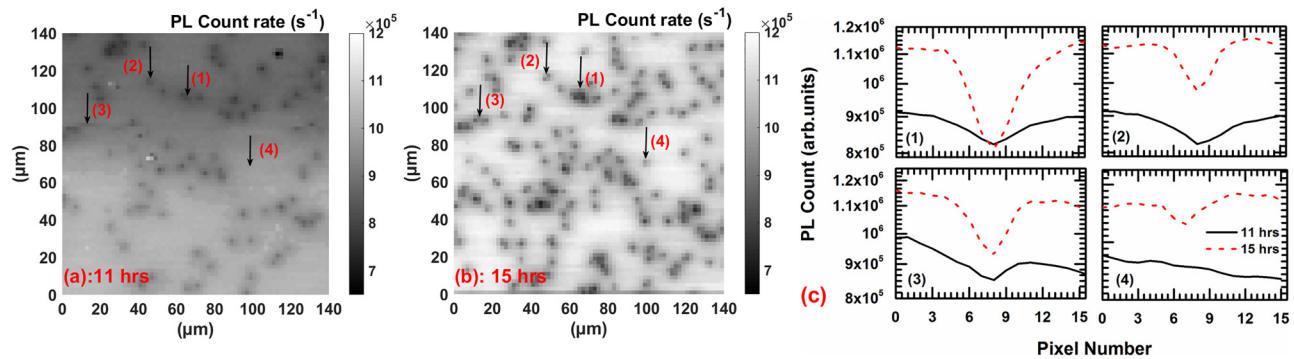


FIG. 6. Micro-PL maps of  $140\mu\text{m} \times 140\mu\text{m}$  areas at location A [as shown in Fig. 4(b)] with the same nucleation anneal at  $650^\circ\text{C}$  for 5 h and, after (a) 11 h and (b) 15 h of precipitate growth anneal at  $1000^\circ\text{C}$ . (c) Line scans of the PL signal at 4 different particles after 11 h and 15 h of precipitate growth anneal. The particle numbers (1)-(4) in (c) correspond to the labels in (a) and (b). The arrows in (a) and (b) illustrate the direction of the line scan.

distinct and relatively larger oxygen precipitates with the apparent areal density of  $4 \times 10^9\text{ cm}^{-2}$ , as shown in the map in Fig. 5(c). However, at position 3, the apparent areal density was only  $1 \times 10^9\text{ cm}^{-2}$ . The radially inhomogeneous distribution of oxygen precipitates in the annealed sample is consistent with the inhomogeneous loss in  $[\text{O}_i]$  obtained by the FTIR measurement, as shown in Sec. III A.

We performed micro-PL mapping at several locations in a radial direction to determine the apparent areal densities of the oxygen precipitates and extracted the inverse lifetime from the PL image for the corresponding locations in a Group II sample. We found the areal precipitate density obtained from the micro-PL maps to be positively correlated with the inverse lifetime derived from the corresponding locations in PL image, as shown in Fig. 5(e). This implies that the majority of recombination active oxygen precipitates which were limiting the lifetime of the sample were detected during micro-PL mapping.

Further, in order to investigate the local features of oxygen precipitates, we mapped at the same location “A,” as shown in the PL image in Fig. 4(b) after 11 h and 15 h of precipitate growth anneal on Group II sample. The maps are shown in Figs. 6(a) and 6(b). Some interesting phenomena were observed in the maps after the two different anneal durations. First, we observed an increase in contrast between the oxygen precipitates and the background PL intensity, as shown in Fig. 6(c), which implied that the oxygen precipitates are more recombination active. This could be due to further growth of the oxygen precipitates. Second, we observed several new particles, such as indicated by “4” in Fig. 6(b). Thus, we found that the areal density of detected oxygen precipitates evidently increased from  $3 \times 10^9\text{ cm}^{-2}$  to  $5 \times 10^9\text{ cm}^{-2}$ . This observation of precipitate growth accentuates the potential value of the micro-PL technique for studying oxygen precipitate evolution. These growth behaviors are difficult to observe using selective etching techniques due to their destructive natures or electron beam induced current (EBIC) measurements due to requirements of p-n junction and metal contact formation.

The apparent increase in oxygen precipitate density might be due to the dissolution of smaller oxygen precipitates with an increase of annealing temperature or duration.<sup>37</sup> During the precipitate growth anneal, the smaller precipitate

nuclei dissolve, leaving only precipitate nuclei larger than a certain critical size for further growth.<sup>20,37</sup> Further, at high temperatures, such as  $1000^\circ\text{C}$ , nucleation of new oxygen precipitates is not likely.<sup>8,37</sup> The distribution thus becomes skewed to larger precipitate sizes as the growth time increases.<sup>20,37</sup> Therefore, some of the nano-scale precipitates, which were undetected during the mapping of the 11 h annealed sample, might have grown to a detectable size after the additional 4 h of annealing, leading to the observed increase in the detected precipitate density.

#### D. The loss in $[\text{O}_i]$ and apparent oxygen precipitate density

Figure 7 presents the apparent areal densities of the oxygen precipitates obtained from the micro-PL maps at several locations in a radial direction and the loss in  $[\text{O}_i]$  calculated from the FTIR after 11 h of precipitate growth anneal. It shows no clear relationship between loss in  $[\text{O}_i]$  and apparent oxygen precipitate density. This could be due to detection limits of the micro-PL, with some of the nano-precipitates remaining undetected during the mapping. Further, the micro-PL mapping is not able to detect the low

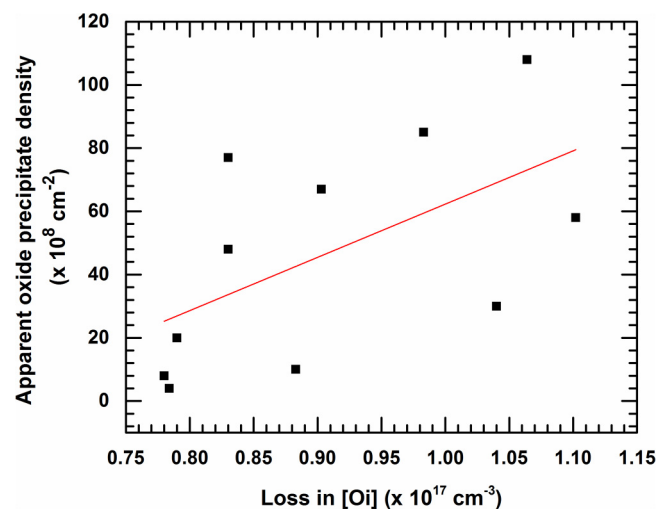


FIG. 7. Apparent oxygen precipitates areal density obtained from the micro-PL maps as a function of loss in  $[\text{O}_i]$  obtained from an FTIR scanning microscope after  $650^\circ\text{C}$ -5 h;  $1000^\circ\text{C}$ -11 h anneal.

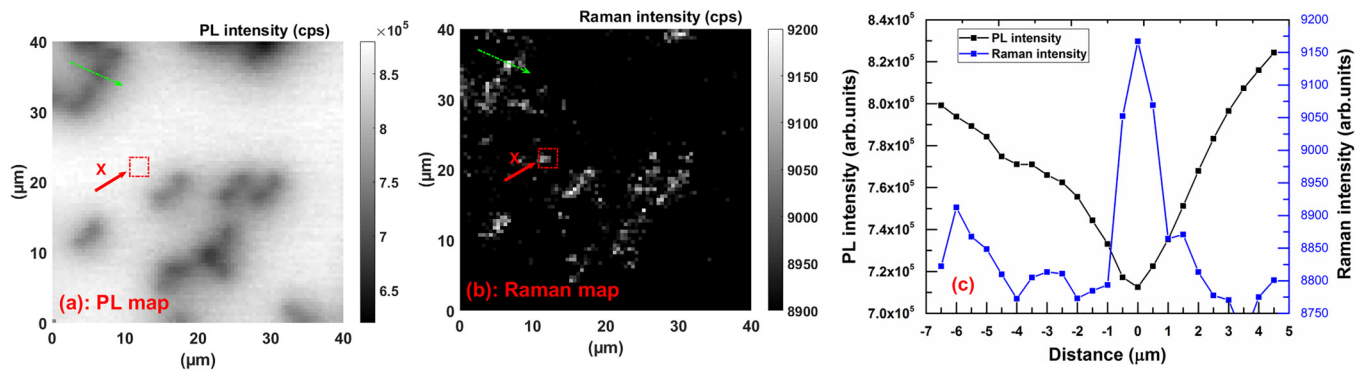


FIG. 8.  $40\mu\text{m} \times 40\mu\text{m}$  micro-PL and micro-Raman maps at location B [as shown in Fig. 4(b)] with the spatial resolution of  $0.5\mu\text{m}$  for a Group II sample. (a) Micro-PL map, (b) micro-Raman map, and (c) spatial profiles of the Raman intensity at  $520\text{ cm}^{-1}$  and band to band PL intensity at  $1130\text{ nm}$  as indicated by green dashed arrow in maps. The green dotted arrows in (a) and (b) illustrate the direction of line scans of the PL and the Raman signals. The red box represents the exact same location in the maps.

recombination active oxygen precipitates due to the very high injection level employed here. Thus, there could be some smaller sized and unstrained/less-active oxygen precipitates which remained undetected in the micro-PL maps, causing the weak correlation observed in Fig. 7.

### E. Micro-Raman map and oxygen precipitates

Figure 8 shows the micro-PL and the micro-Raman maps at the same location “B,” as shown in the PL image in Fig. 4(b). From these two maps, we observe two different phenomena—first, we observed several new oxygen precipitates as indicated by “X” in the micro-Raman map and second, oxygen precipitates were much better resolved in the micro-Raman map. The appearance of new oxygen precipitates in the micro-Raman map implied that the oxygen precipitates were non-uniform in their recombination activity. This could be either due to variations in size,<sup>38</sup> state (strained or unstrained),<sup>39</sup> morphology,<sup>6,40</sup> or concentration of decorating metallic impurities.<sup>6</sup> The absence of an oxygen precipitate as indicated by particle “X” in the micro-PL map is not likely due to its smaller size as it is of comparable size to the detected precipitates, as shown in the micro-Raman map in Fig. 8(b). However, the concentration of metallic impurities decorating particle “X” could be low or it might be less strained. If this hypothesis is true, the recombination activity of particle “X” was weak and remained undetected by micro-PL.<sup>6</sup> To investigate this phenomenon, we performed phosphorus gettering on the sister annealed sample, and interestingly we did not observe any oxygen precipitates in a micro-PL map. However, we could observe the oxygen precipitates on the micro-Raman map (maps are not shown here).

Figure 8(c) presents the line scans of the Raman intensity at  $520\text{ cm}^{-1}$  and the PL intensity at  $1130\text{ nm}$ , at the same precipitates as indicated by dotted arrows in Figs. 8(a) and 8(b). The PL intensity reaches the background value approximately  $12\mu\text{m}$  from the peak intensity, whereas the Raman intensity reaches the background level within  $2\mu\text{m}$ . This is due to the different emission mechanisms of Raman and PL signals: the Raman photons are emitted from the excited electrons which are still bound to their host atoms or molecules, whereas the

PL photons are emitted from the excited carriers which move freely in the material. This reflects the fact that compared with PL, the Raman signal is not affected by the carrier smearing as the excited electrons are confined within their host atoms or molecules.<sup>41</sup> As a result, a micro-Raman map provides a better spatial resolution of the oxygen precipitates as it is not susceptible to carrier smearing.<sup>41</sup> Therefore, oxygen precipitate densities calculated from micro-Raman maps should be better correlated with the loss in  $[\text{O}_i]$  obtained from FTIR measurements. However, to obtain a high signal-to-noise ratio and maintain a high spatial resolution ( $0.5\mu\text{m}$  in this work), relatively long acquisition times in the order of 1–5 s per pixel are required. This results in a total measurement time for a single map on the order of several hours. Therefore, oxygen precipitate densities in this work were determined by micro-PL maps. This highlights the potential value in combining PL and Raman mapping for studying precipitates in silicon materials.

### IV. CONCLUSIONS

We have presented a high spatial resolution investigation of ring defects in two-step annealed Cz-Si wafers using a combination of FTIR scanning microscopy, micro-PL mapping at high injection conditions, and micro-Raman mapping. We observed a direct local correlation between losses in  $[\text{O}_i]$  obtained from scanning FTIR measurements and the inverse lifetime extracted from PL images in a two-step annealed sample. Further, this paper demonstrated the use of micro-PL mapping to investigate ring defects. The high-resolution micro-PL maps successfully resolved the recombination-active individual particles and their distribution within the ring defects due to a combination of higher spatial resolution and reduced carrier smearing at higher injection levels. Our results demonstrate that the ring defects or lifetime striations are indeed due to the cumulative effect of individual oxygen precipitates. Furthermore, the micro-Raman maps confirm that besides the precipitates detected in the micro-PL maps, there are in fact smaller and/or less-active precipitates not revealed by the micro-PL technique due to the carrier smearing. This explains the very weak correlation between the loss in  $[\text{O}_i]$  and apparent precipitate density detected from the micro-PL maps. Therefore, micro-PL and micro-Raman

techniques can be the powerful combination for the study of oxygen precipitates in n-type Cz-Si.

## ACKNOWLEDGMENTS

This work has been supported by the Australian Renewable Energy Agency (ARENA) through the Australian Center for Advanced Photovoltaics (ACAP) and Project Nos. RND009 and RND017. R.B. would like to acknowledge Hang Sio for helpful discussions and Logan Stenlake for FTIR measurements. H.T.N. acknowledges the support of an ACAP Fellowship.

- <sup>1</sup>G. Coletti, P. Manshanden, S. Bernardini, P. C. P. Bronsveld, A. Gutjahr, Z. Hu, and G. Li, *Sol. Energy Mater. Sol. Cells* **130**, 647 (2014).
- <sup>2</sup>K. Marsden, S. Sadamitsu, T. Yamamoto, and T. Shigematsu, *Jpn. J. Appl. Phys.* **34**, 2974 (1995).
- <sup>3</sup>A. Le Donne, S. Binetti, V. Folegatti, and G. Coletti, *Appl. Phys. Lett.* **109**, 033907 (2016).
- <sup>4</sup>J. Haunschild, I. E. Reis, J. Geilker, and S. Rein, *Phys. Status Solidi Rapid Res. Lett.* **5**, 199 (2011).
- <sup>5</sup>J. Vanhellemont, E. Simoen, A. Kaniava, M. Libezny, and C. Claeys, *J. Appl. Phys.* **77**, 5669 (1995).
- <sup>6</sup>J. D. Murphy, K. Bothe, V. V. Voronkov, and R. J. Falster, *Appl. Phys. Lett.* **102**, 042105 (2013).
- <sup>7</sup>J. D. Murphy, R. E. McGuire, K. Bothe, V. V. Voronkov, and R. J. Falster, *Sol. Energy Mater. Sol. Cells* **120**, 402 (2014).
- <sup>8</sup>N. Inoue, J. Osaka, and K. Wado, *J. Electrochem. Soc.* **129**, 2780 (1982).
- <sup>9</sup>I. Fusegawa and H. Yamagishi, *Semicond. Sci. Technol.* **7**, A304–A310 (1992).
- <sup>10</sup>K. Nauka, H. C. Gatos, and J. Lagowski, *Appl. Phys. Lett.* **43**, 241 (1983).
- <sup>11</sup>C. J. Varker, J. D. Whitfield, and P. L. Fejes, in *ASTM Symposium on Silicon Processing* (American Society for Testing and Materials, San Jose, 1982).
- <sup>12</sup>G. Gaspar, G. Coletti, M. Juel, S. Würzner, R. Sondenå, M. Di Sabatino, L. Arnberg, and E. J. Øvrelid, *Sol. Energy Mater. Sol. Cells* **153**, 31–43 (2016).
- <sup>13</sup>B. Mitchell, J. Greulich, and T. Trupke, *Sol. Energy Mater. Sol. Cells* **107**, 75 (2012).
- <sup>14</sup>J. Schön, A. Youssef, S. Park, L. E. Mundt, T. Niewelt, S. Mack, K. Nakajima, K. Morishita, R. Murai, M. A. Jensen, T. Buonassisi, and M. C. Schubert, *J. Appl. Phys.* **120**, 105703 (2016).
- <sup>15</sup>P. Gundel, M. C. Schubert, W. Kwapil, J. Schön, M. Reiche, H. Savin, M. Yli-Koski, J. A. Sans, G. Martinez-Criado, W. Seifert, W. Warta, and E. R. Weber, *Phys. Status Solidi Rapid Res. Lett.* **3**, 230 (2009).
- <sup>16</sup>C. Sun, H. T. Nguyen, F. E. Rougieux, and D. Macdonald, *J. Cryst. Growth* **460**, 98 (2017).
- <sup>17</sup>P. Gundel, F. D. Heinz, M. C. Schubert, J. A. Giesecke, and W. Warta, *J. Appl. Phys.* **108**, 033705 (2010).
- <sup>18</sup>P. Gundel, M. C. Schubert, F. D. Heinz, R. Woehl, J. Benick, J. A. Giesecke, D. Suwito, and W. Warta, *Nanoscale Res. Lett.* **6**, 197 (2011).
- <sup>19</sup>G. Sarau, S. Christiansen, M. Holla, and W. Seifert, *Sol. Energy Mater. Sol. Cells* **95**, 2264–2271 (2011).
- <sup>20</sup>K. F. Kelton, R. Falster, D. Gambaro, M. Olmo, M. Cornara, and P. F. Wei, *J. Appl. Phys.* **85**, 8097 (1999).
- <sup>21</sup>P. Wang, L. Chang, L. J. Demer, and C. J. Varker, *J. Electrochem. Soc.* **131**, 1948 (1984).
- <sup>22</sup>W. Kaiser, P. H. Keck, and C. F. Lange, *Phys. Rev.* **101**, 1264 (1956).
- <sup>23</sup>T. Trupke, R. Bardos, M. Schubert, and W. Warta, *Appl. Phys. Lett.* **89**, 044107 (2006).
- <sup>24</sup>K. Schinke, K. Bothe, P. Christian Peest, J. Schmidt, and R. Brendel, *Appl. Phys. Lett.* **104**, 081915 (2014).
- <sup>25</sup>C. Claeys, E. Simoen, and J. Vanhellemont, *J. Phys. III Fr.* **7**, 1469 (1997).
- <sup>26</sup>V. V. Voronkov and R. Falster, *J. Cryst. Growth* **204**, 462 (1999).
- <sup>27</sup>V. V. Voronkov, *J. Cryst. Growth* **59**, 625–643 (1982).
- <sup>28</sup>H. Zimmermann and H. Ryssel, *MRS Proc.* **262**, 31 (1992).
- <sup>29</sup>K. S. Choe, *J. Cryst. Growth* **262**, 35 (2004).
- <sup>30</sup>A. J. R. De Kock, P. J. Roksnoer, and P. G. T. Boonen, *J. Cryst. Growth* **28**, 125 (1975).
- <sup>31</sup>J. A. Burton, R. C. Prim, and W. P. Slichter, *J. Chem. Phys.* **21**, 1987 (1953).
- <sup>32</sup>K. Kakimoto and H. Ozoe, *Comput. Mater. Sci.* **10**, 127 (1998).
- <sup>33</sup>S. Kawanishi, S. Togawa, K. Izunome, K. Terashima, and S. Kimura, *J. Cryst. Growth* **152**, 266 (1995).
- <sup>34</sup>T. Abe, *J. Cryst. Growth* **24–25**, 463 (1974).
- <sup>35</sup>A. J. R. De Kock, *Appl. Phys. Lett.* **16**, 100 (1970).
- <sup>36</sup>R. Basnet, F. E. Rougieux, C. Sun, S. P. Phang, C. Samundsett, R. Einhaus, J. Degoulange, and D. Macdonald, *IEEE J. Photovoltaics* **8**, 990 (2018).
- <sup>37</sup>R. Falster, M. Cornara, D. Gambaro, M. Olmo, and M. Pagani, *Solid State Phenom.* **57–58**, 123 (1997).
- <sup>38</sup>M. Porrini and P. Tessariol, *Mater. Sci. Eng. B* **73**, 244 (2000).
- <sup>39</sup>J. D. Murphy, M. Al-Amin, K. Bothe, M. Olmo, V. V. Voronkov, and R. J. Falster, *J. Appl. Phys.* **118**, 215706 (2015).
- <sup>40</sup>J. D. Murphy, K. Bothe, M. Olmo, V. V. Voronkov, and R. J. Falster, *J. Appl. Phys.* **110**, 053713 (2011).
- <sup>41</sup>C. Hu, Q. Chen, F. Chen, T. H. Gfroerer, M. W. Wanlass, and Y. Zhang, *Light Sci. Appl.* **7**, 23 (2018).